Utsu aftershock productivity law explained from geometric operations on the permanent static stress field of mainshocks

Arnaud Mignan*

Institute of Geophysics, Swiss Federal Institute of Technology, Zurich

Address: ETHZ, Institute of Geophysics, NO H66, Sonneggstrasse 5, CH-8092 Zurich

Correspondence to: arnaud.mignan@sed.ethz.ch

Abstract: The aftershock productivity law is an exponential function of the form $K \propto \exp(\alpha M)$ with K the number of aftershocks, M the mainshock magnitude, and $\alpha \approx \ln(10)$ the productivity parameter. This law remains empirical in nature although it has also been retrieved in static stress simulations. Here, we explain this law based on Solid Seismicity, a geometrical theory of seismicity where seismicity patterns are described by mathematical expressions obtained from geometric operations on a permanent static stress field. We first validate the Solid Seismicity Postulate that relates seismicity density to a static stress step function. We show that it yields a power exponent $q = 1.96 \pm 0.01$ for the power-law spatial linear density distribution of aftershocks, once uniform noise is added to the static stress field, in agreement with observations. We then recover the exponential function of the productivity law with a break in scaling obtained between small and large M, with $\alpha = 1.5\ln(10)$ and $\ln(10)$, respectively, in agreement with results from previous static stress simulations. Possible biases of aftershock selection, verified to exist in Epidemic-Type Aftershock Sequence (ETAS) simulations, may explain the lack of break in scaling observed in seismicity catalogues. The existence of the theoretical kink remaining to be proven, we describe how to estimate the Solid Seismicity parameters (activation density δ_+, aftershock solid envelope r_* and background stress amplitude range Δo_*) for large M values only.

1. Introduction

Aftershocks, the most robust patterns observed in seismicity, are characterized by three empirical laws, which are functions of time (e.g., Utsu et al., 1995; Mignan, 2015), space (e.g., Richards-Dinger et al., 2010; Moradpour et al., 2014) and mainshock magnitude (Utsu, 1970a; b; Ogata, 1988). The present study focuses on the

latter relationship, i.e., the Utsu aftershock productivity law, which describes the total number of aftershocks K produced by a mainshock of magnitude M as

$$K(M) = K_0 \exp[\alpha(M - m_0)] \quad (1)$$

with m_0 the minimum magnitude cutoff (Utsu, 1970b; Ogata, 1988). This relationship was originally proposed by Utsu (1970a; b) by combining two other empirical laws, the Gutenberg-Richter relationship (Gutenberg and Richter, 1944) and Båth's law (Båth, 1964), respectively:

$$\begin{cases} N(\geq m) = A\exp[-\beta(m - m_0)] \\ N(\geq M - \Delta m_B) = 1 \end{cases} \quad (2)$$

with β the magnitude size ratio (or $b = \beta/\ln(10)$ in base-10 logarithmic scale) and Δm_B the magnitude difference between the mainshock and its largest aftershock, such that

$$K(M) = N(\geq m_0|M) = \exp(-\beta \Delta m_B)\exp[\beta(M - m_0)] \quad (3)$$

with $K_0 = \exp(-\beta \Delta m_B)$ and $\alpha \equiv \beta$. Eq. (3) was only implicit in Utsu (1970a) and not exploited in Utsu (1970b) where K_0 was fitted independently of the value taken by Båth's parameter Δm_B. The α-value was in turn decoupled from the β–value in later studies (e.g., Seif et al. (2017) and references therein).

Although it seems obvious that Eq. (1) can be explained geometrically if the volume of the aftershock zone is correlated to the mainshock surface area S with

$$S(M) = 10^{M-4} = \exp[\ln(10)(M - 4)] \quad (4)$$

(Kanamori and Anderson, 1975; Yamanaka and Shimazaki, 1990; Helmstetter, 2003), there is so far no analytical, physical expression of Eq. (1) available. Although Hainzl et al. (2010) retrieved the exponential behavior in numerical simulations where aftershocks were produced by the permanent static stress field of mainshocks of different magnitudes, it remains unclear how K_0 and α relate to the underlying physical parameters.

The aim of the present article is to explain the Utsu aftershock productivity equation (Eq. 1) by applying a geometrical theory of seismicity (or "Solid Seismicity"), which has already been shown to effectively explain other empirical laws of both natural and induced seismicity from simple geometric operations on a permanent static stress field (Mignan, 2012; 2016a). The theory is applied here for the first time to the case of aftershocks.

2. Physical Expression of the Aftershock Productivity Law

2.1. Demonstration by Solid Seismicity

"Solid Seismicity", a geometrical theory of seismicity, is based on the following Postulate (Mignan et al., 2007; Mignan, 2008, 2012; 2016a):

> **Solid Seismicity Postulate (SSP):** *Seismicity can be strictly categorized into three regimes of constant spatiotemporal densities – background δ_0, quiescence δ_- and activation δ_+ (with $\delta_- \ll \delta_0 \ll \delta_+$) - occurring respective to the static stress step function:*
>
> $$\delta(\sigma) = \begin{cases} \delta_- & , \sigma < -\Delta o_* \\ \delta_0 & , \sigma \leq |\pm\Delta o_*| \\ \delta_+ & , \sigma > \Delta o_* \end{cases} \quad (5)$$
>
> *with Δo_* the background stress amplitude range.*

Based on this Postulate, Mignan (2012) demonstrated the power-law behavior of precursory seismicity in agreement with the observed time-to-failure equation (Varnes, 1989), while Mignan (2016a) demonstrated both the observed parabolic spatiotemporal front and the linear relationship with injection-flow-rate of induced seismicity (Shapiro and Dinske, 2009). It remains unclear whether the SSP has a

physical origin or not. If not, it would still represent a reasonable approximation of the linear relationship between event production and static stress field in a simple clock-change model (Hainzl et al., 2010) (Fig. 1a) (for the validation of the SSP from the observed spatial distribution of aftershocks, see section 2.2). The power of Eq. (5) is that it allows defining seismicity patterns in terms of "solids" described by the spatial envelope $r_* = r(\sigma = \pm\Delta o_*)$. The spatiotemporal rate of seismicity is then a mathematical expression defined by the density of events δ times the volume characterized by r_* (see previous demonstrations in Mignan et al. (2007) and Mignan (2011; 2012; 2016a) where simple algebraic expressions were obtained).

In the case of aftershocks, we define the static stress field of the mainshock by

$$\sigma(r) = -\Delta\sigma_0 \left[\left(1 - \frac{c^3}{(r+c)^3} \right)^{-1/2} - 1 \right] \quad (6)$$

with $\Delta\sigma_0 < 0$ the mainshock stress drop, c the crack radius and r the distance from the crack. Eq (6) is a simplified representation of stress change from slip on a planar surface in a homogeneous elastic medium. It takes into account both the square root singularity at crack tip and the $1/r^3$ falloff at higher distances (Dieterich, 1994) (Fig. 1b). It should be noted that this radial static stress field does not represent the geometric complexity of Coulomb stress fields (Fig. 2a). However we are here only interested in the general behavior of aftershocks with Eq. (6) retaining the first-order characteristics of this field (i.e., on-fault seismicity; Fig. 2b), which corresponds to the case where the mainshock relieves most of the regional stresses and aftershocks occur on optimally oriented faults. It is also in agreement with observations, most aftershocks being located on and around the mainshock fault traces in Southern California (Fig. 2c; see section "Observations & Model Fitting"). The occasional

cases where aftershocks occur off-fault (e.g., Ross et al., 2017) can be explained by the mainshock not relieving all of the regional stress (King et al., 1994) (Fig. 2d).

For $r_* = r(\sigma = \Delta o_*)$, Eq. (6) yields the aftershock solid envelope of the form:

$$r_*(c) = \left\{ \frac{1}{\left[1-\left(1-\frac{\Delta\sigma_*}{\Delta\sigma_0}\right)^{-2}\right]^{1/3}} - 1 \right\} c = Fc \tag{7}$$

, function of the crack radius c and of the ratio between background stress amplitude range Δo_* and stress drop $\Delta\sigma_0$ (Fig. 1c). With $\Delta\sigma_0$ independent of earthquake size (Kanamori and Anderson, 1975; Abercrombie and Leary, 1993) and Δo_* assumed constant, r_* is directly proportional to c with proportionality constant, or stress factor, F (Eq. 7). Geometrical constraints due to the seismogenic layer width w_0 then yield

$$c(M) = \begin{cases} \left(\frac{S(M)}{\pi}\right)^{1/2} & , S(M) \leq \pi w_0^2 \\ w_0 & , S(M) > \pi w_0^2 \end{cases} \tag{8}$$

with S the rupture surface defined by Eq. (4) and c becoming an effective crack radius (Kanamori and Anderson, 1975) (Fig. 1d). Note that the factor of 2 (i.e., using w_0 instead of $w_0/2$) comes from the free surface effect (e.g., Kanamori and Anderson, 1975; Shaw and Scholz, 2001).

The aftershock productivity $K(M)$ is then the activation density δ_+ times the volume $V_*(M)$ of the aftershock solid. For the case in which the mainshock relieves most of the regional stress, stresses are increased all around the rupture (King et al., 1994), which is topologically identical to stresses increasing radially from the rupture plane (Fig. 2a-b). It follows that the aftershock solid can be represented by a volume of contour $r_*(M)$ from the rupture plane geometric primitive, i.e., a disk or a rectangle, for small and large mainshocks respectively. This is illustrated in Figure 3a-b and can be generalized by

$$V_*(M) = 2r_*(M)S(M) + \frac{\pi}{2} r_*^2(M)d \tag{9}$$

where d is the distance travelled around the geometric primitive by the geometric centroid of the semi-circle of radius $r_*(M)$ (i.e., Pappus's Centroid Theorem), or

$$d = \begin{cases} 2\pi\left(c(M) + \frac{4}{3\pi}r_*(M)\right) & , c(M) + r_*(M) \le \frac{w_0}{2} \\ 2w_0 & , \ c(M) + r_*(M) > \frac{w_0}{2} \end{cases} \quad (10)$$

For the disk, the volume (Eq. 9) corresponds to the sum of a cylinder of radius $c(M)$ and height $2r_*(M)$ (first term) and of half a torus of major radius $c(M)$ and minus radius $r_*(M)$ (second term). For the rectangle, the volume is the sum of a cuboid of length $l(M)$ (i.e., rupture length), width w_0 and height $2r_*(M)$ (first term) and of a cylinder of radius $r_*(M)$ and height w_0 (second term; see red and orange volumes, respectively, in Figure 3a-c). Finally inserting Eqs. (7), (8) and (10) into (9), we obtain

$$K(M) = \delta_+ \begin{cases} \left[\frac{2F}{\sqrt{\pi}} + F^2\sqrt{\pi}\left(1 + \frac{4}{3\pi}F\right)\right] S^{3/2}(M) & , S(M) \le \left(\frac{w_0\sqrt{\pi}}{2(1+F)}\right)^2 \\ \frac{2F}{\sqrt{\pi}} S^{3/2}(M) + F^2 w_0 S(M) & \left(\frac{w_0\sqrt{\pi}}{2(1+F)}\right)^2 < S(M) \le \pi w_0^2 \\ 2F w_0 S(M) + \pi F^2 w_0^3 & , S(M) > \pi w_0^2 \end{cases} \quad (11)$$

which is represented in Figure 3d. Considering the two main regimes only (small versus large mainshocks) and inserting Eq. (4) into (11), we get

$$K(M) = \delta_+ \begin{cases} \left[\frac{2F}{\sqrt{\pi}} + F^2\sqrt{\pi}\left(1 + \frac{4}{3\pi}F\right)\right] \exp\left[\frac{3\ln(10)}{2}(M-4)\right] & , \text{small } M \\ 2F w_0 \exp[\ln(10)(M-4)] + \pi F^2 w_0^3 & , \text{large } M \end{cases} \quad (12)$$

which is a closed-form expression of the same form as the original Utsu productivity law (Eq. 1). Note that K and δ_+ are both, implicitly, function of the selected minimum aftershock magnitude threshold m_0.

Here, we predict that the α-value decreases from $3\ln(10)/2 \approx 3.45$ to $\ln(10) \approx 2.30$ when switching regime from small to large mainshocks (or from 1.5 to 1 in base-10 logarithmic scale). It should be noted that Hainzl et al. (2010) observed the same

150 break in scaling in static stress transfer simulations, which corroborates our analytical
151 findings. For large *M*, the scaling is fundamentally the same as in Eq. (4). Since that
152 relation also explains the slope of the Gutenberg-Richter law (see physical
153 explanation given by Kanamori and Anderson (1975)), it follows that $\alpha \equiv \beta$, which is
154 also in agreement with the original formulation of Utsu (1970a; b) (Eq. 3).
155
156 *2.2. Validation of the Solid Seismicity Postulate*
157 The SSP predicts a step-like spatial behavior of aftershocks for an idealized
158 smooth static stress field (Fig. 4a-b), which is in disagreement with real aftershock
159 observations. A number of studies have shown that the spatial linear density
160 distribution of aftershocks ρ is well represented by a power-law, expressed as
161 $\rho(r) \propto r^{-q}$ (13)
162 with *r* the distance from the mainshock and *q* the power-law exponent. This parameter
163 ranges over $1.3 \leq q \leq 2.5$ (Felzer and Brodsky, 2006; Lipiello et al., 2009; Marsan and
164 Lengliné, 2010; Richards-Dinger et al., 2010; Shearer, 2012; Gu et al., 2013;
165 Moradpour et al., 2014; van der Elst and Shaw, 2015). Although Felzer and Brodsky
166 (2004) suggested a dynamic stress origin for aftershocks, their results were later on
167 discredited by Richards-Dinger et al. (2010). Most of the studies cited above suggest
168 that the *q*-value is explained from a static stress process (as for the examples of
169 aftershocks shown to be dynamically triggered (e.g., Fan and Shearer, 2016), they are
170 too few to alter the aftershock productivity law and too remote to be consistently
171 defined as aftershocks in cluster methods).
172 In a more realistic setting, the static stress field must be heterogeneous (due to
173 the occurrence of previous events and other potential stress perturbations). We
174 therefore simulate the static stress field by adding a uniform random component

bounded over $\pm\Delta o_*$ following Mignan (2011) (see also King and Bowman, 2003). Note that any deviation above Δo_* would be flattened to Δo_* over time by temporal diffusion (so-called "historical ghost static stress field" in Mignan, 2016a). Figure 4c shows the resulting stress field and Figure 4d the predicted aftershock spatial density. Adding uniform noise blurs the contour of the aftershock solid, switching the aftershock spatial density from a step function (Fig. 4b) to a power-law (Fig. 4d). We fit Eq. (13) to the simulated data using the Maximum Likelihood Estimation (MLE) method with $r_{min} = r_*$ (Clauset et al., 2009) and find $q = 1.96 \pm 0.01$, in agreement with the aftershock literature.

3. Observations & Model Fitting

3.1. Data

We consider the case of Southern California and extract aftershock sequences from the relocated earthquake catalog of Hauksson et al. (2012) defined over the period 1981-2011, using the nearest-neighbor method (Zaliapin et al., 2008) (used with its standard parameters originally calibrated for Southern California, considering only the first aftershock generation). Only events with magnitudes greater than $m_0 = 2.0$ are considered (a conservative estimate following results of Tormann et al. (2014); saturation effects immediately after the mainshock are negligible when considering entire aftershock sequences; Helmstetter et al. (2005)).

3.2. Aftershock spatial density distribution

Figure 5a represents the spatial linear density distribution of aftershocks $\rho(r)$ for the four largest strike-slip mainshocks in Southern California: 1987 M=6.6 Superstition Hills, 1992 M=7.3 Landers, 1999 M=7.1 Hector Mine, and 2010 M=7.2

El Mayor. The distance between mainshock and aftershocks is calculated as $r = \sqrt{(x - x_0)^2 + (y - y_0)^2}$ with (x, y) the aftershock coordinates and (x_0, y_0) the coordinates of the nearest point to the mainshock fault rupture (as depicted in Figure 2c). The dashed black lines shown in Figure 5a are visual guides to q = 1.96, showing that the SSP is compatible with real aftershock observations.

Comparing Figure 5a to Figure 4d suggests that r_* can be roughly estimated from the spatial linear density plot, being the maximum distance r at which the plateau ends, here leading to $r_* \approx 1$ km. This parameter is constant for different large M values since both w_0 and $\Delta\sigma_0$ are constant while $\Delta\sigma_*$ is also *a priori* a constant. We can then estimate the ratio $\Delta\sigma_*/\Delta\sigma_0$ from Eq. (7). However the result is ambiguous due to uncertainties on the width w_0. For w_0 = {5, 10, 15} km, we get $\Delta\sigma_*/\Delta\sigma_0$ ={-0.54, -1.01, -1.38}.

As for the plateau value $\rho(r < r_*)$, it provides an estimate of the aftershock activation density δ_+ with

$$\delta_+ = \frac{\rho(M, r<r_*)}{\exp[\ln(10)(M-4)]} \quad (14)$$

a volumetric density, i.e. the linear density ρ normalized by the mainshock rupture area (Eq. 4). Due to the fluctuations in $\rho(r < r_*)$, δ_+ will be estimated from the productivity law instead (see section 3.3) and $\rho(r < r_*)$ then estimated from Eq. (14) (horizontal dashed colored lines), as detailed below.

It should be noted that we consider only the first-generation aftershocks to avoid ρ heterogeneities from secondary aftershock clusters occurring off-fault. An example of such heterogeneity/anisotropy is illustrated by the Landers-Big Bear case (Fig. 2c; dotted colored curve on Fig. 5a). Those cases are not systematic and therefore not considered in the aftershock productivity law. However they are also

due to static stress changes (e.g., King et al., 1994) with the anisotropic effects explainable by Solid Seismicity through the concept of "historical ghost static stress field" (Mignan, 2016a).

3.3. Aftershock productivity law

The observed number n of aftershocks of magnitude $m \geq m_0$ produced by a mainshock of magnitude M (for a total of N mainshocks) in Southern California is shown in Figures 5b (for large $M \geq 6$) and 6a (for the full range $M \geq m_0$). We fit Eq. (1) to the data using the MLE method with the log-likelihood function

$$LL(\theta; X = \{n_i; i = 1, ..., N\}) = \sum_{i=1}^{N} [n_i \ln[K_i(\theta)] - K_i(\theta) - \ln(n_i!)] \quad (15)$$

for a Poisson process. Inserting Eq. (1) in Eq. (15) yields

$$LL(\theta = \{K_0, \alpha\}; X) = \ln(K_0) \sum_{i=1}^{N} n_i + \alpha \sum_{i=1}^{N} [n_i (M_i - m_0)] - K_0 \sum_{i=1}^{N} \exp[\alpha (M_i - m_0)] - \sum_{i=1}^{N} \ln(n_i!) \quad (16)$$

(note that the last term can be set to 0 during LL maximization). For Southern California, we obtain $\alpha_{MLE} = 2.32$ (1.01 in $\log_{10}$ scale) and $K_0 = 0.025$ when considering large $M \geq 6$ mainshocks only to avoid the issues of scaling break and data dispersion at lower magnitudes. This result, represented by the black solid line on Figure 5b, is in agreement with previous studies in the same region (e.g., Helmstetter, 2003; Helmstetter et al., 2005; Zaliapin and Ben-Zion, 2013; Seif et al., 2017) and with $\alpha = \ln(10) \approx 2.30$ predicted for large mainshocks in Solid Seismicity (Eq. 12). Moreover we find a bulk $\beta_{MLE} = 2.34$ (1.02 in $\log_{10}$ scale) (Aki, 1965), in agreement with $\alpha \equiv \beta$.

Let us now rewrite the Solid Seismicity aftershock productivity law (Eq. 12) by only considering the large M case and injecting $r_* = Fw_0$ (by combining Eqs. 7-8). We get

$$K(M > M_{break}) = \delta_+\{2r_*\exp[ln(10)(M-4)] + \pi r_*^2 w_0\} \quad (17)$$

The role of w_0 is illustrated in Figure 5b for different values (dashed and dotted curves) and shown to be insignificant for large M values. Therefore Eq. (17) can be approximated to

$$K(M > M_{break}) \approx 2\delta_+ r_*\exp[ln(10)(M-4)] \quad (18)$$

By analogy with Eq. (1), we get

$$\delta_+ = \frac{K_0\exp[\ln(10)(4-m_0)]}{2r_*} \quad (19)$$

With $r_* \approx 1$ km estimated from $\rho(r)$ (section 3.2) and $K_0 = 0.025$, we obtain $\delta_+ = 1.23$ events/km^3 for $m_0 = 2$. We then get back the plateau $\rho(r < r_*)$ for different M values from Eq. (14), as shown in Figure 5a (horizontal dashed colored lines). Although based on limited data, this result suggests that the activation parameter δ_+ is constant (at least for large M) in Southern California. Note that if $\rho(r < r_*)$ was well constrained, it could have been estimated jointly with r_* from Figure 5a to predict the aftershock productivity law of Figure 5b without further fitting required (hence removing K_0 from the equation, K_0 having no physical meaning in Solid Seismicity).

4. Role of aftershock selection on productivity scaling-break

We tested the following piecewise model to identify any break in scaling at smaller M, as predicted by Eq. (12):

$$K(M) = \begin{cases} K_0 \frac{\exp[\ln(10)(M_{break}-m_0)]}{\exp\left[\frac{3}{2}\ln(10)(M_{break}-m_0)\right]} \exp\left[\frac{3}{2}\ln(10)(M-m_0)\right] & , M \le M_{break} \\ K_0\exp[\ln(10)(M-m_0)] & , M > M_{break} \end{cases} \quad (20)$$

but with the best MLE result obtained for $M_{break} = m_0$, suggesting no break in scaling in the aftershock productivity data, as observed in Figure 6a. Final parameter

estimates are $\alpha_{MLE} = 1.95$ (in $\log_{10}$ scale) and $K_0 = 0.141$ for the full mainshock magnitude range $M \geq m_0$ (dotted line), subject to high scattering at low M values.

We now identify whether the lack of break in scaling in aftershock productivity observed in earthquake catalogues could be an artefact related to the aftershock selection method. We run Epidemic-Type Aftershock Sequence (ETAS) simulations (Ogata, 1988; Ogata and Zhuang, 2006), with the seismicity rate

$$\begin{cases} \lambda(t,x,y) = \mu(t,x,y) + \sum_{i:t_j<t} K(M_i) f(t-t_i) g(x-x_i, y-y_i|M_i) \\ f(t) = c^{p-1}(p-1)(t+c)^{-p} \\ g(x,y|M) = \frac{1}{\pi}\left(de^{\gamma(M-m_0)}\right)^{q-1}\left(x^2+y^2+de^{\gamma(M-m_0)}\right)^{-q}(q-1) \end{cases} \quad (21)$$

Aftershock sequences are defined by power laws, both in time and space (for an alternative temporal function, see Mignan (2015; 2016b); the spatial power-law distribution is in agreement with Solid Seismicity in the case of a heterogeneous static stress field – see section 2.2). μ is the Southern California background seismicity, as defined by the nearest-neighbor method (with same t, x, y and m). We fix the ETAS parameters to $\theta = \{c = 0.011$ day, $p = 1.08$, $d = 0.0019$ km^2, $q = 1.47$, $\gamma = 2.01$, $\beta = 2.29$, $K_0 = 0.08\}$, following the fitting results of Seif et al. (2017) for the Southern California relocated catalog and $m_0 = 2$ (see their Table 1). However, we define the productivity function $K(M)$ from Eq. (20) with $M_{break} = 5$. Examples of ETAS simulations are shown in Figure 6b for comparison with the observed Southern California time series. Figure 6c allows us to verify that the simulated aftershock productivity is kinked at M_{break}, as defined by Eq. (20).

We then select aftershocks from the ETAS simulations with the nearest-neighbor method. Figure 4d represents the estimated aftershock productivity, which has lost the break in scaling originally implemented in the simulations (with an underestimated $\alpha_{MLE} = 2.07$ as observed in the real case for $M \geq m_0$). Note that a

295 similar result is obtained when using a windowing method (Gardner and Knopoff,
296 1974). This demonstrates that the theoretical break in scaling predicted in the
297 aftershock productivity law can be lost in observations due to an aftershock selection
298 bias, all declustering techniques assuming continuity over the entire magnitude range.
299 While such a bias is possible, it yet does not prove that the break in scaling exists. The
300 fact that a similar break in scaling was obtained in independent Coulomb stress
301 simulations (Hainzl et al., 2010) however provides high confidence in our results.
302 One other possible explanation for lack of scaling break is that our
303 demonstration assumes moment magnitudes while the Southern California catalogue
304 is in local magnitudes. Deichmann (2017) demonstrated that while $M_L \propto M_w$ at large
305 M, $M_L \propto 1.5M_w$ at smaller *M* values. This could in theory cancel the kink in real data.
306 However the scaling break predicted by Deichmann (2017) occurs at several
307 magnitude units below the geometric scaling break expected by Solid Seismicity,
308 invalidating this second option for mid-range magnitudes *M*.
309
310 **5. Conclusions**
311 In the present study, a physical closed-form expression defined from
312 geometric and static stress parameters was proposed (Eq. 12) to explain the empirical
313 Utsu aftershock productivity law (Eq. 1). This demonstration, combined to the
314 previous ones made by the author to explain precursory accelerating seismicity and
315 induced seismicity (Mignan, 2012; 2016b), suggests that most empirical laws
316 observed in seismicity populations can be explained by simple geometric operations
317 on a permanent static stress field. In all these demonstrations, the main physical
318 parameters remain the same, i.e. the activation density δ_+ (also δ_- and δ_0), the
319 background stress amplitude range Δo_*, and the solid envelope r_* which describes the

geometry of the "seismicity solid" (Fig. 3a-b). Further studies will be needed to evaluate whether the δ_+ and Δo_* parameters are universal or region-specific and if the same values apply to different types of seismicity at a same location.

Although the Solid Seismicity Postulate (SSP) (Eq. 5) remains to be proven, it is so far a rather convenient and pragmatic assumption to determine the physical parameters that play a first-order role in the behavior of seismicity. The similarity of the SSP-simulated and observed values of the power-law exponent q of the aftershock spatial density distribution suggests that the SSP is a proper approach (Figs. 4d-5a). It is also complementary to the more common simulations of static stress loading (King and Bowman, 2003) and static stress triggering (Hainzl et al., 2010).

Analytic geometry, providing both a visual representation and an analytical expression of the problem at hand (Fig. 3), represents a new approach to try to understand better the behavior of seismicity. Its current limitation in the case of aftershock analysis consists in assuming that the static stress field is radial and described by Eq. (6) (Dieterich, 1994), which is likely only valid for mainshocks relieving most of the regional stresses and with aftershocks occurring on optimally oriented faults (King et al., 1994). More complex, second-order, stress behaviors might explain part of the scattering observed around Eq. (1) (Fig. 6a), such as overpressure due to trapped high-pressure gas for example (Miller et al., 2004 – see also Mignan (2016a) for an overpressure field due to fluid injection). Other $\sigma(r)$ formulations could be tested in the future, the only constraint on generating so-called seismicity solids being the use of the postulated static stress step function of Eq. (5) (i.e., the Solid Seismicity Postulate, SSP).

Finally, the disappearance of the predicted scaling break in the aftershock productivity law once declustering is applied (Fig. 6) indicates that more work is

345 required in that domain. Only a declustering technique that does not dictate a constant
346 scaling at all *M* will be able to identify rather a scaling break really exists or not.
347
348 *Acknowledgments:* I thank N. Wetzler and two anonymous reviewers for their
349 valuable comments.
350
351 **References**
352 Abercrombie, R. and Leary, P.: Source parameters of small earthquakes recorded at
353 2.5 km depth, Cajon Pass, Southern California: Implications for earthquake
354 scaling, Geophys. Res. Lett., 20, 1511-1514, 1993.
355 Aki, K.: Maximum Likelihood Estimate of b in the Formula log N = a-bM and its
356 Confidence Limits, Bull. Earthq. Res. Instit., 43, 237-239, 1965.
357 Båth, M.: Lateral inhomogeneities of the upper mantle, Tectonophysics, 2, 483-514,
358 1965.
359 Clauset, A., Shalizi, C. R. and Newman, M. E. J.: Power-Law Distributions in
360 Empirical Data, SIAM Review, 51, 661-703, doi: 10.1137/070710111, 2009.
361 Deichmann, N.: Theoretical Basis for the Observed Break in M_L/M_w Scaling between
362 Small and Large Earthquakes, Bull. Seismol. Soc. Am., 107, doi:
363 10.1785/0120160318, 2017.
364 Dieterich, J.: A constitutive law for rate of earthquake production and its application
365 to earthquake clustering, J. Geophys. Res., 99, 2601-2618, 1994.
366 Fan, W. and Shearer, P. M.: Local near instantaneously dynamically triggered
367 aftershocks of large earthquakes, Science, 353, 1133-1136, 2016.

368 Felzer, K. R. and Brodsky, E. E.: Decay of aftershock density with distance indicates
369 triggering by dynamic stress, Nature, 441, 735-738, doi: 10.1038/nature04799,
370 2006.
371 Gardner, J. K. and Knopoff, L.: Is the sequence of earthquakes in Southern California,
372 with aftershocks removed, Poissonian?, Bull. Seismol. Soc. Am., 64, 1363-1367,
373 1974.
374 Gu, C., Schumann, A. Y., Baisesi, M. and Davidsen, J.: Triggering cascades and
375 statistical properties of aftershocks, J. Geophys. Res. Solid Earth, 118, 4278-4295,
376 doi: 10.1002/jgrb.50306, 2013.
377 Gutenberg, B. and Richter, C. F.: Frequency of earthquakes in California, Bull.
378 Seismol. Soc. Am., 34, 185-188, 1944.
379 Hainzl, S., Brietzke, G. B. and Zöller, G.: Quantitative earthquake forecasts resulting
380 from static stress triggering, J. Geophys. Res., 115, B11311, doi:
381 10.1029/2010JB007473, 2010.
382 Hauksson, E., Yang, W. and Shearer, P. M.: Waveform Relocated Earthquake Catalog
383 for Southern California (1981 to June 2011), Bull. Seismol. Soc. Am., 102, 2239-
384 2244, doi: 10.1785/0120120010, 2012.
385 Helmstetter, A.: Is Earthquake Triggering Driven by Small Earthquakes?, Phys. Rev.
386 Lett., 91, doi: 10.1102/PhysRevLett.91.058501, 2003.
387 Helmstetter, A., Kagan, Y. Y. and Jackson, D. D. : Importance of small earthquakes
388 for stress transfers and earthquake triggering, J. Geophys. Res., 110, B05S08, doi:
389 10.1029/2004JB003286, 2005.
390 Kanamori, H. and Anderson, D. L.: Theoretical basis of some empirical relations in
391 seismology, Bull. Seismol. Soc. Am., 65, 1073-1095, 1975.

King, G. C. P., Stein, R. S. and Lin, J.: Static Stress Changes and the Triggering of Earthquakes, Bull. Seismol. Soc. Am., 84, 935-953, 1994.

King, G. C. P. and Bowman, D. D.: The evolution of regional seismicity between large earthquakes, J. Geophys. Res., 108, 2096, doi: 10.1029/2001JB000783, 2003.

Lin, J. and Stein, R. S.: Stress triggering in thrust and subduction earthquakes, and stress interaction between the southern San Andreas and nearby thrust and strike-slip faults, J. Geophys. Res., 109, B02303, doi: 10.1029/2003JB002607, 2004.

Lippiello, E., de Arcangelis, J. and Godano, C.: Role of Static Stress Diffusion in the Spatiotemporal Organization of Aftershocks, Phys. Rev. Lett., 103, 038501, doi: 10.1103/PhysRevLett.103.038501, 2009.

Marsan, D. and Lengliné, O.: A new estimation of the decay of aftershock density with distance to the mainshock, J. Geophys. Res., 115, B09302, doi: 10.1029/2009JB007119, 2010.

Miller, S. A., Collettini, C., Chiaraluce, L., Cocco, M., Barchi, M. and Kaus, B. J. P.: Aftershocks driven by a high-pressure CO_2 source at depth, Nature, 427, 724-727

Mignan, A., King, G. C. P. and Bowman, D.: A mathematical formulation of accelerating moment release based on the stress accumulation model, J. Geophys. Res., 112, B07308, doi: 10.1029/2006JB004671, 2007.

Mignan, A.: Non-Critical Precursory Accelerating Seismicity Theory (NC PAST) and limits of the power-law fit methodology, Tectonophysics, 452, 42-50, doi: 10.1016/j.tecto.2008.02.010, 2008.

Mignan, A.: Retrospective on the Accelerating Seismic Release (ASR) hypothesis: Controversy and new horizons, Tectonophysics, 505, 1-16, doi: 10.1016/j.tecto.2011.03.010, 2011.

Mignan, A.: Seismicity precursors to large earthquakes unified in a stress accumulation framework, Geophys. Res. Lett., 39, L21308, doi: 10.1029/2012GL053946, 2012.

Mignan, A.: Modeling aftershocks as a stretched exponential relaxation, Geophys. Res. Lett., 42, 9726-9732, doi: 10.1002/2015GL066232, 2015.

Mignan, A.: Static behaviour of induced seismicity, Nonlin. Processes Geophys., 23, 107-113, doi: 10.5194/npg-23-107-2016, 2016a.

Mignan, A.: Reply to "Comment on 'Revisiting the 1894 Omori Aftershock Dataset with the Stretched Exponential Function' by A. Mignan" by S. Hainzl and A. Christophersen, Seismol. Res. Lett., 87, 1134-1137, doi: 10.1785/0220160110, 2016b.

Moradpour, J., Hainzl, S. and Davidsen, J.: Nontrivial decay of aftershock density with distance in Souther California, J. Geophys. Res. Solid Earth, 119, 5518-5535, doi: 10.1002/2014JB010940, 2014.

Ogata, Y.: Statistical Models for Earthquake Occurrences and Residual Analysis for Point Processes, J. Am. Stat. Assoc., 83, 9-27, 1988.

Ogata, Y. and Zhuang, J.: Space-time ETAS models and an improved extension, Tectonophysics, 413, 13-23, doi: 10.1016/j.tecto.2005.10.016, 2006.

Richards-Dinger, K., Stein, R. S. and Toda, S.: Decay of aftershock density with distance does not indicate triggering by dynamic stress, Nature, 467, 583-586, doi: 10.1038/nature09402, 2010.

Ross, Z. E., Hauksson, E. and Ben-Zion, Y.: Abundant off-fault seismicity and orthogonal structures in the San Jacinto fault zone, Sci. Adv., 3, doi: 10.1126/sciadv.1601946, 2017.

Seif, S., Mignan, A., Zechar, J. D., Werner, M. J. and Wiemer, S.: Estimating ETAS: The effects of truncation, missing data, and model assumptions, J. Geophys. Res. Solid Earth, 121, 449-469, doi: 10.1002/2016JB012809, 2017.

Shapiro, S. A. and Dinske, C.: Scaling of seismicity induced by nonlinear fluid-rock interaction, J. Geophys. Res., 114, B09307, doi: 10.1029/2008JB006145, 2009.

Shaw, B. E. and Scholz, C. H.: Slip-length scaling in large earthquakes: Observations and theory and implications for earthquake physics, Geophys. Res. Lett., 28, 2995-2998, 2001.

Shearer, P. M.: Space-time clustering of seismicity in California and the distance dependence of earthquake triggering, J. Geophys. Res., 117, B10306, doi: 10.1029/2012JB009471, 2012.

Toda, S., Stein, R. S., Richards-Dinger, K. and Bozkurt, S.: Forecasting the evolution of seismicity in southern California: Animations built on earthquake stress transfer, J. Geophys. Res., 110, B05S16, doi: 10.1029/2004JB003415, 2005.

Tormann, T., Wiemer, S. and Mignan, A.: Systematic survey of high-resolution b value imaging along Californian faults: inference on asperities, J. Geophys. Res. Solid Earth, 119, 2029-2054, doi: 10.1002/2013JB010867, 2014.

Utsu, T.: Aftershocks and Earthquake Statistics (1): Some Parameters Which Characterize an Aftershock Sequence and Their Interrelations, J. Faculty Sci. Hokkaido Univ. Series 7 Geophysics, 3, 129-195, 1970a.

Utsu, T.: Aftershocks and Earthquake Statistics (2): Further Investigation of Aftershocks and Other Earthquake Sequences Based on a New Classification of Earthquake Sequences, J. Faculty Sci. Hokkaido Univ. Series 7 Geophysics, 3, 197-266, 1970b.

464 Utsu, T., Ogata,, Y. and Matsu'ura, R. S.: The Centenary of the Omori Formula for a
465 Decay Law of Aftershock Activity, J. Phys. Earth, 43, 1-33, 1995.
466 van der Elst, N. J. and Shaw, B. E.: Larger aftershocks happen farther away:
467 Nonseparability of magnitude and spatial distributions of aftershocks, Geophys.
468 Res. Lett., 42, 5771-5778, doi: 10.1002/2015GL064734, 2015.
469 Varnes, D. J.: Predicting Earthquakes by Analyzing Accelerating Precursory Seismic
470 Activity, Pure Appl. Geophys., 130, 661-686, 1989.
471 Yamanaka, Y. and Shimazaki, K.: Scaling Relationship between the Number of
472 Aftershocks and the Size of the Main Shock, J. Phys. Earth, 38, 305-324, 1990.
473 Zaliapin, I., Gabrielov, A., Keilis-Borok, V. and Wong, H.: Clustering Analysis of
474 Seismicity and Aftershock Identification, Phys. Rev. Lett., 101, 018501, doi:
475 10.1103/PhysRevLett.101.018501, 2008.
476 Zaliapin, I. and Ben-Zion, Y.: Earthquake clusters in southern California I:
477 Identification and stability, J. Geophys. Res. Solid Earth, 118, 2847-2864, doi:
478 10.1002/jgrb.50179, 2013.
479
480 **Figures**

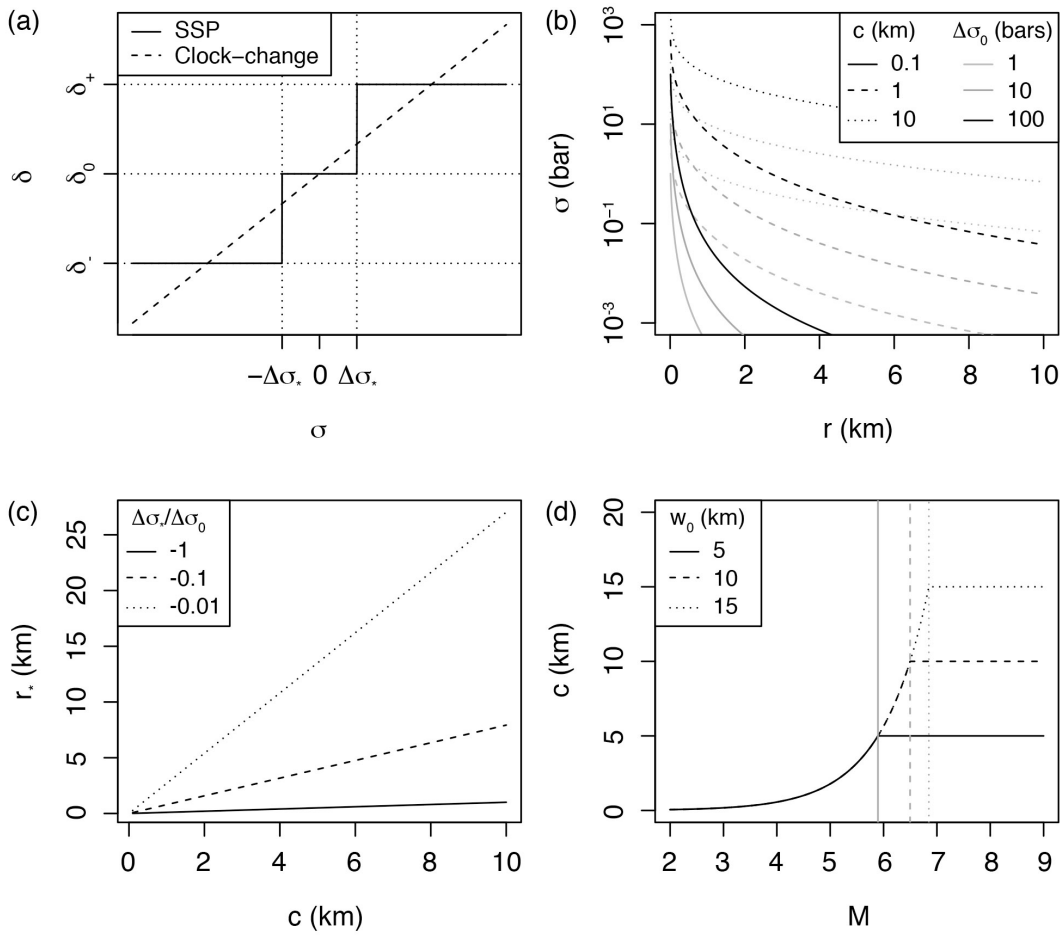

481

482 **Figure 1.** Definition of the aftershock solid envelope in a permanent static stress field:
483 (a) Event density stress step-function $\delta(\sigma)$ (Eq. 5) of the Solid Seismicity Postulate
484 (SSP) in comparison to the linear clock-change model; (b) Static stress σ versus
485 distance r for different effective crack radii c and rupture stress drops $\Delta\sigma_0$ (Eq. 6); (c)
486 Linear relationship between effective crack radius c and aftershock solid envelope
487 radius r_* for different $\Delta\sigma_*/\Delta\sigma_0$ ratios (Eq. 7); (d) Relationship between mainshock
488 magnitude M and effective crack radius c for different seismogenic widths w_0 (Eq. 8).
489

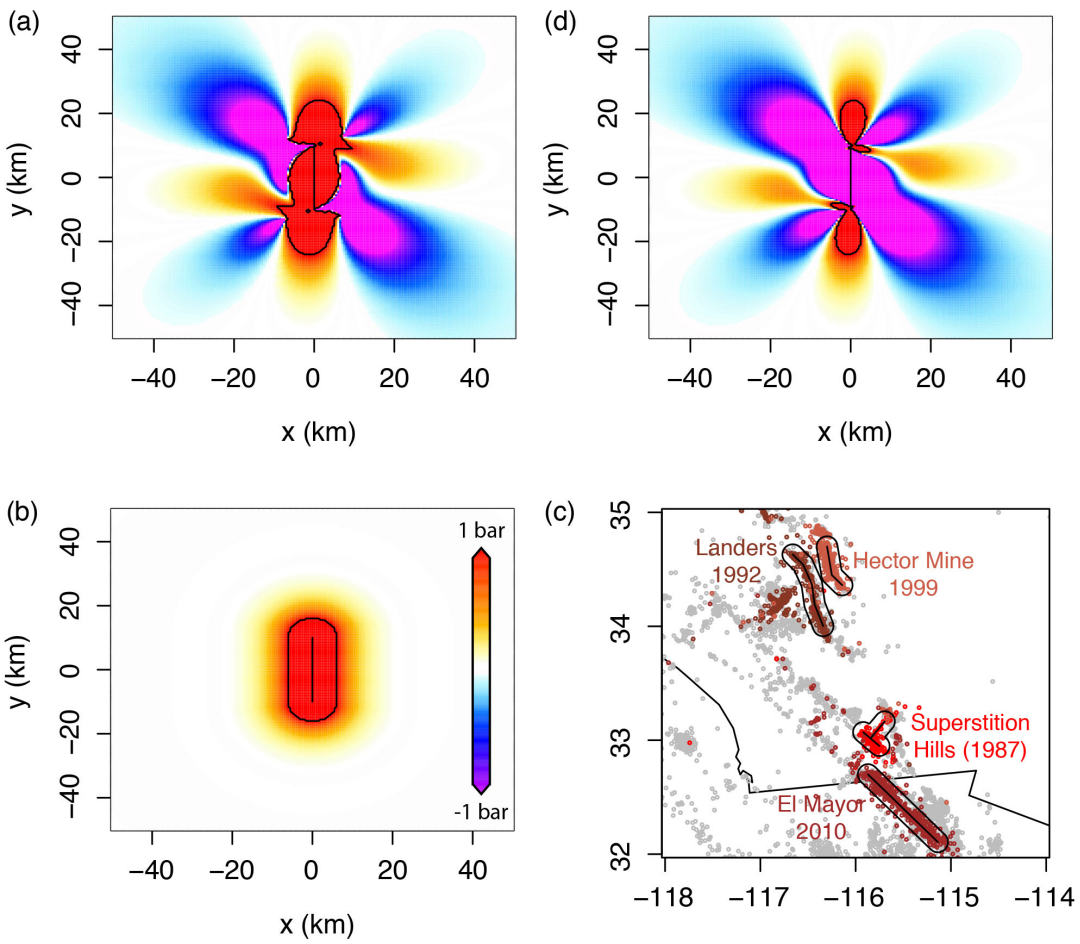

490

491 **Figure 2.** Possible static stress fields and inferred aftershock spatial distribution: (a)
492 Right-lateral Coulomb stress field for optimally oriented faults, where the mainshock
493 relieves all of the regional stresses σ_r = 10 bar, with $\Delta\sigma_0 \approx -Gs/L \approx$ - 10 bar (G =
494 $3.3.10^5$ bar the shear modulus, s = 0.6 m the slip, L = 20 km the fault length, and w =
495 10 km the fault width); (b) Radial static stress field computed from Eq. (6) with $\Delta\sigma_0$ =
496 -10 bar and $c = \sqrt{(Lw)/\pi}$ for consistency with (a); (c) Aftershock distribution of the
497 largest strike-slip events in the Southern California relocated catalog, identified here
498 as all events occurring within one day of the mainshock (see Data section 3.1); (d)
499 Right-lateral Coulomb stress field for optimally oriented faults, where the mainshock
500 relieves only a fraction of the regional stresses σ_r = 100 bar with $\Delta\sigma_0$ = -10 bar (same
501 rupture as in (a)) – The black contour represents 1 bar in (a), (b) and (d), and a 10 km

distance from rupture in (c). Coulomb stress fields of (a) and (d) were computed using the Coulomb 3 software (Lin and Stein, 2004; Toda et al., 2005).

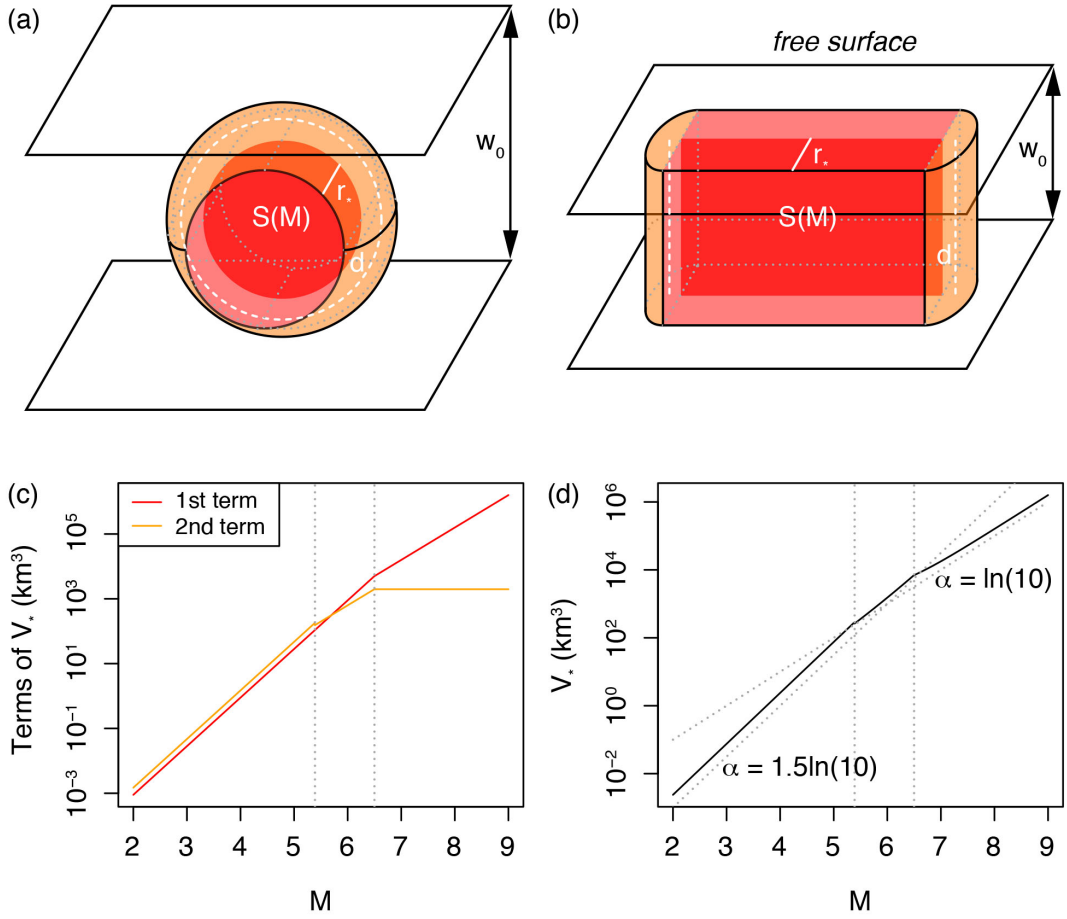

Figure 3. Geometric origin of the aftershock productivity law: (a) Sketch of the aftershock solid for a small mainshock rupture represented by a disk; (b) Sketch of the aftershock solid for a large mainshock rupture represented by a rectangle; (c) Relative role of the two terms of Eq. (9), here with w_0 = 10 km and $\frac{\Delta\sigma_*}{\Delta\sigma_0}$ = -0.1 (to first estimate c and r_* from Eqs. 8 and 7, respectively); (d) Aftershock productivity law (normalized by δ_+) predicted by Solid Seismicity (Eq. 11). This relationship is of the same form as the Utsu productivity law (Eq. 1) for large M (see text for an explanation of the lack

513 of break in scaling in Eq. 1 for small M). Dotted vertical lines represent M for

514 $c(M) + r_*(M) = \frac{w_0}{2}$ and $S(M) = \pi w_0^2$, respectively.

515

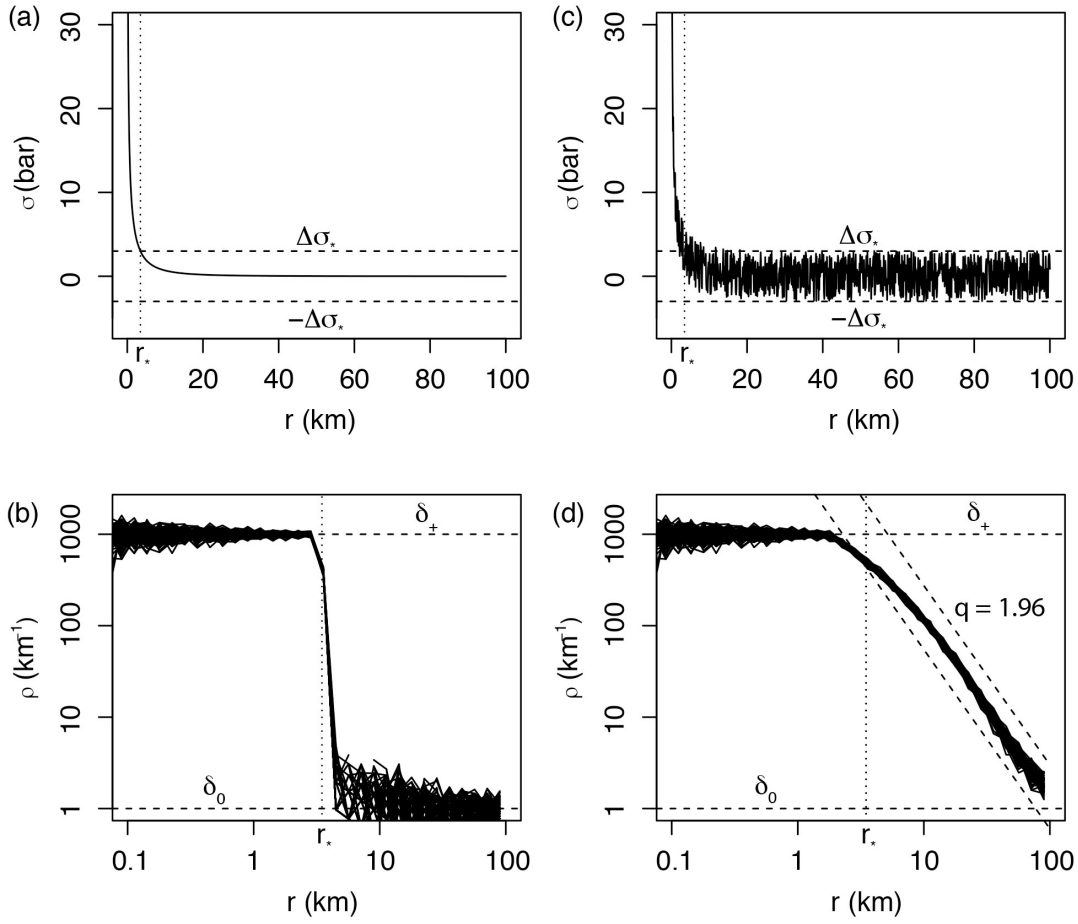

516

517 **Figure 4.** Spatial distribution of aftershocks following the SSP. (a) Smooth static

518 stress field as a function of distance r from the mainshock, with $\Delta\sigma_0$ = -10 bar and c =

519 10 km (Eq. 6); (b) Step-like aftershock spatial linear density $\rho(r)$ with δ_+ = 1000

520 events per km, δ_0 = 1 event per km and $\Delta\sigma_*$ = -0.3$\Delta\sigma_0$ (*ad-hoc* ratio yielding r_* = 3.5

521 km; Eq. (7) – event distances sampled from the $\delta(r)$ distribution, repeated 100 times).

522 Such distribution is not observed in Nature; (c) Same as (a) but with random uniform

523 noise representative of spatial heterogeneities added to the regional stress field; (d)

524 Power-law-like aftershock spatial linear density $\rho(r)$ with power exponent MLE

estimate $q = 1.96$, representative of real aftershock observations (see Fig. 5a), due to the addition of uniform noise to the static stress field.

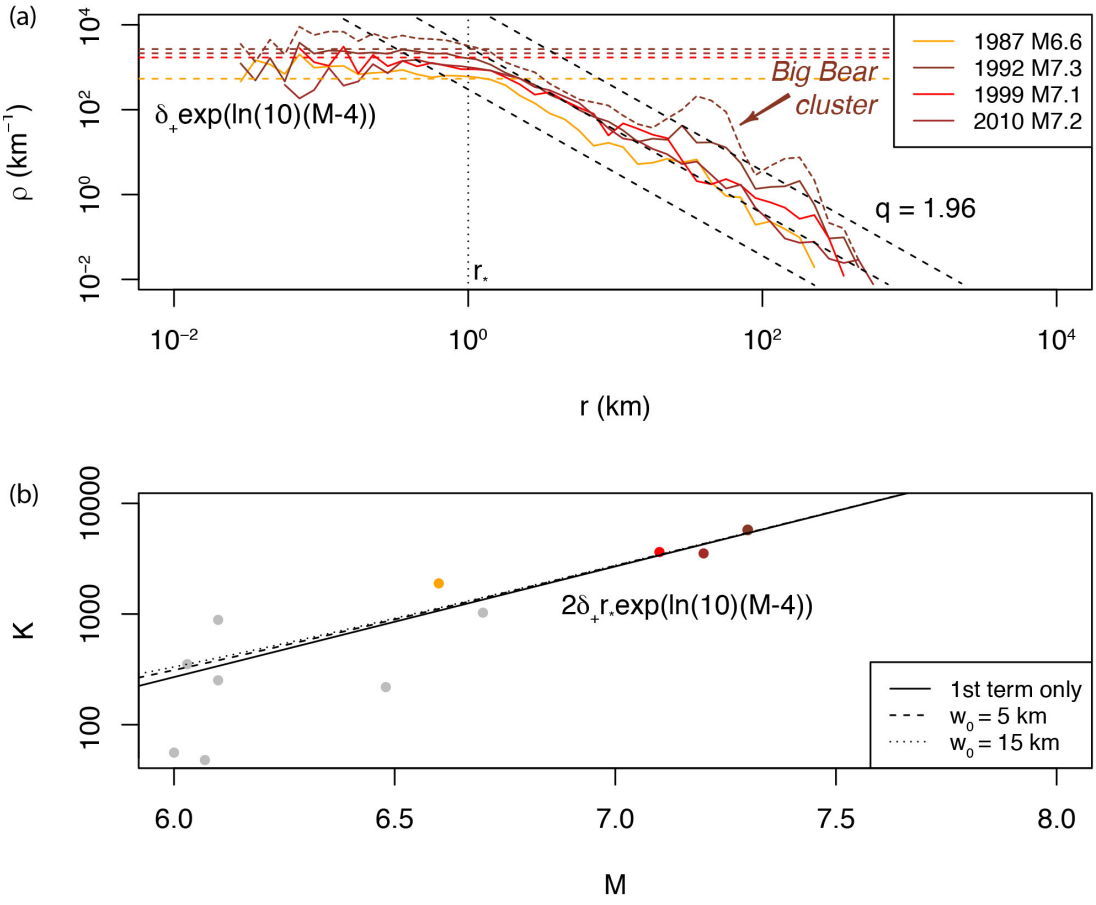

Figure 5. Estimating the Solid Seismicity parameters from the spatial distribution of aftershocks: (a) Spatial linear density distribution $\rho(r)$ of aftershocks for the four largest strike-slip mainshocks in Southern California (with first-generation aftershocks only; the density distribution comprising all aftershocks generated by the Landers mainshock is represented by the dotted curve to illustrate the type of spatial heterogeneity, such as the Big Bear cluster, not considered in the present study – see also Fig. 2c). The Solid Seismicity parameters $r_* = 1$ km and $\delta_+(m_0 = 2) = 1.23$ events/km^3 can be retrieved from the observed plateau $\rho(r < r_*)$, in agreement with the SSP (see Fig. 4d). Note that the spatial power-law decay at high r is similar to the one

expected by the SSP in the case of a static stress field with additive uniform noise (expected q = 1.96 represented by the dashed black lines); (b) Aftershock productivity K for $M > 6$. The curves represent the productivity law as defined by Solid Seismicity (Eq. 17) for different w_0 values (first term only corresponds to $w_0 = 0$; Eq. 18).

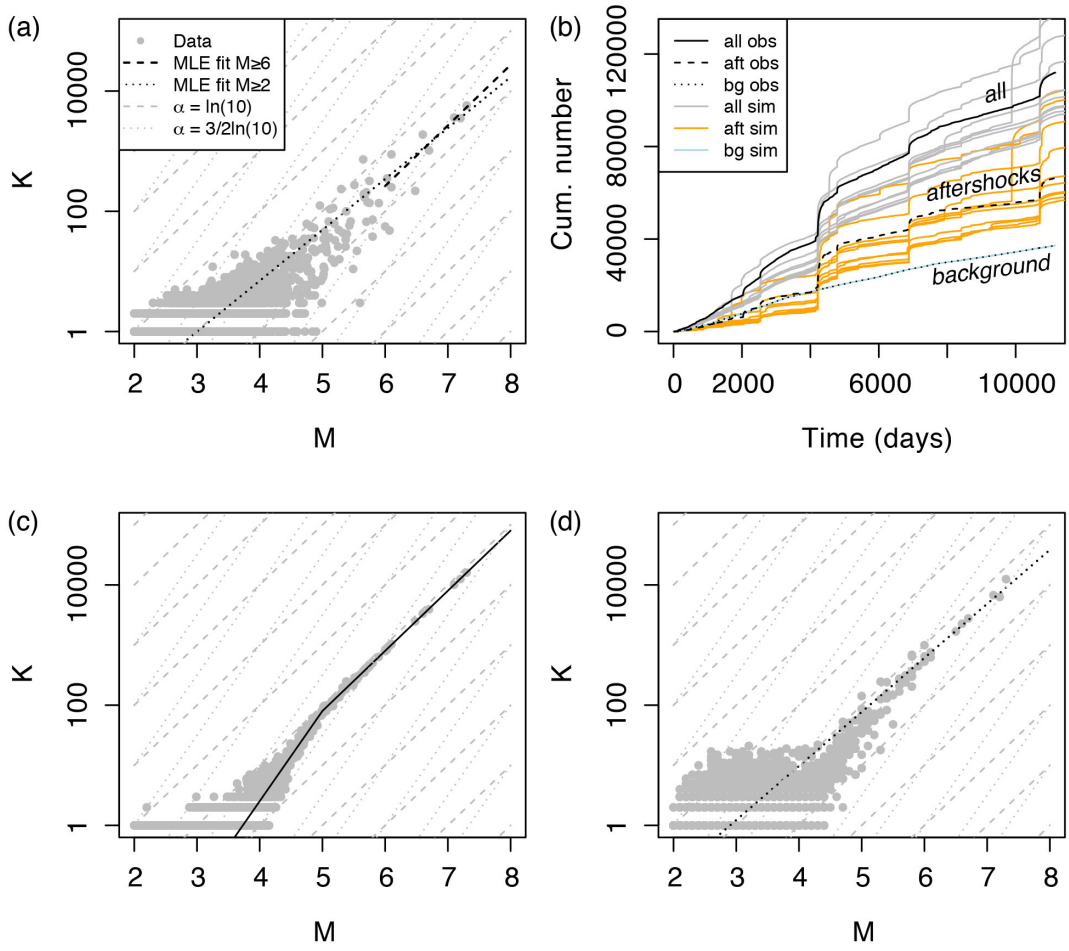

Figure 6. Aftershock productivity defined as the number of aftershocks $K(m_0 = 2)$ per mainshock of magnitude M: (a) Observed aftershock productivity in Southern California with aftershocks selected using the nearest-neighbor method; (b) Seismicity time series with distinction made between background events and aftershocks, observed ("obs", in black) and ETAS-simulated ("sim", colored); (c) True simulated aftershock productivity with kink, defined from Eq. (20); (d)

550 Retrieved simulated aftershock productivity with aftershocks selected using the
551 nearest-neighbor method - Data points in (a), (c) and (d) are represented by grey dots;
552 the model MLE fits are represented by the dashed and dotted black lines for $M \geq 6$
553 and $M \geq m_0$, respectively; dashed and dotted grey lines are visual guides to α =
554 3/2ln(10) and ln(10), respectively.
555